Nanocomposite Ag:TiN thin films for dry biopotential electrodes

Paulo Pedrosa, Diogo Machado, Claudia de Jesus Lopes, Eduardo Alves, Nuno Barradas, Nicolas Martin, Francisco Macedo, Carlos Fonseca, Filipe Vaz

Ag:TiN NANOCOMPOSITE THIN FILMS FOR DRY EEG BIO-ELECTRODES

P. Pedrosa[1,2,3], C. Lopes[3], D. Machado[1], E. Alves[4], N.P. Barradas[4], N. Martin[5], F. Macedo[3], C. Fonseca[1,2], F. Vaz[3*]

[1]SEG-CEMUC – Department of Mechanical Engineering, University of Coimbra, Portugal

[2]Universidade do Porto, Faculdade de Engenharia, Departamento de Engenharia Metalúrgica e de Materiais, Rua Roberto Frias, s/n, 4200-465 Porto, Portugal

[3]Centro de Física, Universidade do Minho, 4710-057 Braga, Portugal

[4]Instituto Tecnológico Nuclear, Deptº. Física, E.N. 10, 2686-953 Sacavém, Portugal

[5]Institut FEMTO-ST (UMR CNRS 6174 – Université de Franche Comté – CNRS – ENSMM – UTBM), ENSMM 26 Chemin de l'Epitaphe, F-25030 Besançon Cedex, France

ABSTRACT

Silver-doped titanium nitride (Ag:TiN) thin films were deposited by PVD in a wide range of compositions with Ag contents ranging from 0 to ~50 at.%, on silicon and glass substrates, aiming at studying their potential application as EEG bio-electrodes. The coatings were characterized regarding their composition, electrical resistivity, morphology, structure and thermal properties. The sputtered films behaviour can be consistently divided into three clear zones, defined mainly by the amount of Ag incorporated. To finish latter with everybody's contribution...

Keywords: Electroencephalography; Bio-electrodes; Silver-doping; RBS; XRD; Resistivity.

*To whom all correspondence should be sent (fvaz@fisica.uminho.pt)

1. INTRODUCTION

Electroencephalography (EEG) is the recording of the brain electrical activity along the scalp, namely the potential fluctuations between its different areas [1]. EEG is nowadays the most widely used brain imaging technique, as it provides excellent time-resolution of brain activity and offers significant advantages over competing state of the art technologies, like MRI (magnetic resonance imaging) and CT (computerized tomography), both in terms of cost and space requirements. The conventional EEG acquisition set-up relies on the use of well-known silver/silver chloride (Ag/AgCl) electrodes. These are considered the gold standard electrodes, as they are non-polarizable and reveal excellent reliability, displaying low and almost frequency independent skin-contact impedance values, in the order of a few tens of $k\Omega.cm^2$ [2]. However, a previous skin preparation and a gel paste application are needed before the exam in order to lower the skin/electrode impedance. This preparation is time consuming, uncomfortable to the patient and requires trained staff. Furthermore, some patients have developed severe allergic reactions to the common used gel pastes [3] and the risk of short-circuiting adjacent electrodes due to gel running can be, in some cases, relatively high.

In order to avoid these and other related drawbacks of the conventional Ag/AgCl electrodes, a new class of devices is being investigated in the group, for which no previous skin preparation or gel application is needed, the so-called “dry” electrodes. In these electrodes, the sensors are based on inert-like materials, either metallic-like or even of insulating type [3,4]. In a previous work [5], the authors investigated a type of dry electrode sensor, based in a titanium nitride (TiN) thin film, deposited on a titanium substrate. Despite the promising results, these electrodes, as well as other similar dry electrodes [6,7], are quite rigid, which can give rise to an incorrect and uncomfortable electrode contact, due to the inherent irregular nature of the human scalp. In addition, taking into account that an EEG recording set-up involves the use of 128 or even 256 electrodes in a single exam, the use of lighter, cheaper and more comfortable electrodes would translate in numerous advantages, when in comparison with the standard Ag/AgCl ones.

The use of polymer-based electrodes, namely the flexible ones, would fill in this gap, as they would surpass most of the problems stated above. Recently, several authors have focused on the development of flexible dry electrodes [8-11]. However, there are still some drawbacks inherent to the dry electrodes, namely higher impedances at low frequencies and they are also more susceptible to movement artefacts than the standard wet Ag/AgCl ones [12].

Taking all this into account, the present work aims at studying sputtered Ag:TiN nanocomposite thin films, and assess their suitability to be used as flexible dry EEG electrodes. Reactive DC magnetron sputtering is commonly accepted as one of the most versatile and less expensive techniques, being widely accepted as able to produce fairly high deposition rates and compact coatings, when compared to other techniques. TiN is an electrically conductive coating, with an excellent chemical stability in most media and outstanding mechanical properties, which led to a very broad range of applications, including those in the biomedical area [13,14]. Furthermore, TiN is biocompatible, but it is also a relatively hard and high modulus material, thus unable to withstand large deformations (in fact, most metallic films withstand less than 10% of deformation [15-22]), giving rise to mechanical failure of the coatings, which, in turn, is highly undesirable when the objective is to produce flexible electrodes, that are supposed to adapt to the human scalp. The inclusion of silver, due to its intrinsic characteristics (especially the low Young's modulus and high conductivity [23]), in TiN films may offer the possibility to tailor the Young's modulus of the coating [24], opening a wide range of possible applications, namely those related with the coating of flexible devices such as polymers. Furthermore, silver addition may also allow the tailoring of the materials electrical conductivity [25], which may be of crucial importance in any electrode-based applications. Finally, silver is inherently antimicrobial [26-28], particularly in its nanocrystalline form [29,30] and has the ability to stabilize the electrochemical potential [31], which is of major importance in any application that may involve human body or human bio-signal characterization. Starting with both TiN and silver characteristics, the main goal of the present work is to provide a detailed study on the influence of silver addition to titanium nitride, in order to

optimize the deposition conditions to obtain conductive and mechanically suitable films to coat polymeric-type substrates and with enough bactericide character that may give the as-prepared thin films a set of characteristics to be used in EEG bio-electrodes.

2. EXPERIMENTAL DETAILS

Ag:TiN films were deposited on glass and silicon (100) substrates by reactive DC magnetron sputtering, in a laboratory-sized deposition system. All substrates were sonicated and cleaned with ethanol just before each deposition. The films were prepared with the substrate holder positioned at 70 mm from the Ti/Ag composite target. A DC current density of 100 $A.m^{-2}$ was applied to the composite target, composed of titanium (99.96 at. % purity) and silver pellets (0.8x0.8 cm^2 and1 mm thick pellets glued on the outside of the target) distributed symmetrically along the erosion area. The total surface area of the silver pallets varied between 0.75 to 8.3 cm^2. A gas atmosphere composed of argon + nitrogen was used. The argon flow was kept constant at 60 sccm for all depositions, as well as the nitrogen flow rate, which was set at 5 sccm (corresponding to a partial pressure of 3.4×10^{-2} Pa). The working pressure was approximately constant during the depositions, varying only slightly between 0.35 and 0.38 Pa. No bias voltage was used, and the deposition temperature was maintained approximately constant at 100 ºC during the films' growth. A thermocouple was placed close to the surface of the "substrate holder" on the plasma side (not in direct contact, since depositions were done in rotation mode), and the temperature was monitored during the entire film deposition time. A delay time of five minutes was used before positioning the surface of the samples in front of the Ti/Ag target in order to avoid film contamination resulting from previous depositions (which may have resulted in some target poisoning), and also to assure a practically constant deposition temperature during film growth.

The atomic composition of the as-deposited samples was measured by Rutherford Backscattering Spectroscopy (RBS) using (1.4, 2.3) MeV and (1.4, 2) MeV for the proton and ^4He beams, respectively. Three detectors were used; one located at a scattering angle of 140º and two pin-diode

detectors located symmetrical to each other, both at 165º. Measurements were made for two sample tilt angles, 0º and 30º. Composition profiles for the as-deposited samples were determined using the software NDF [32]. For the ^{14}N, ^{16}O and ^{28}Si data, the cross-sections given by Gurbich were used [33]. The area analysed was about 0.5×0.5 mm^2. The uncertainty in the N concentrations is around 5 at. %. The structure and phase distribution of the coatings were assessed by X-ray diffraction (XRD), using a Bruker AXS Discover D8 diffractometer, operating with Cu K_α radiation and in a Bragg-Brentano configuration. The XRD patterns were deconvoluted and fitted with a Voigt function to determine the structural characteristics of the films, such as the peak position (2θ), the full width at half maximum (FWHM) and the crystallite size. Morphological features of the samples were probed by scanning electron microscopy (SEM), carried out in a FEI Quanta 400FEG ESEM microscope operating at 15 keV. The resistivity measurements were done using the four-probe van der Pauw method [34]. The thermal characteristics of the coatings were accessed by IR radiometry. The measurement system used is externally controlled by software and consists basically in three main parts: excitation, detection and amplification. The amplification is controlled by a pre-amplifier and a two-phase Lock-in amplifier (SR 830 DSP). The amplitude and phase lag relative to the modulated excitation, as a function of the heating modulation frequency, giving information on the thermal wave's properties, are recorded by the lock-in and stored in the main computer. Further details on the technique can be found elsewhere [F. Macedo et al., J. Phys. D: Appl. Phys. 45 (2012) 105301.].

3. RESULTS AND DISCUSSION

3.1. Discharge characteristics: target potential and deposition rates

In order to study the kinetics and the deposition-related features, the evolution of the target potential during the film growth, as well as the final growth rate were firstly characterized. Figure 1 shows the evolution of these two characteristics as a function of the area of the Ag pellets placed on the target. From the analysis of the plot in Fig. 1 it is possible to observe that the amount of silver in

the target (illustrated by the increasing area/number of the pellets placed in the target erosion zone) results in a three-fold variation type, which will be further noted as films prepared within Zones I, II and III. Within Zone I, the prepared thin films can be described as within a TiN-like zone, where both target potential and deposition rates are somewhat similar due to the small area of Ag exposed. However, a small change in the behaviour of the studied parameters can be seen with further small additions of Ag. Within Zone II, which can be indexed to the incorporation of intermediate amounts of Ag in the target erosion zone, a small increase of both growth rate and discharge voltage are observed, although not very different from the values within Zone I. As for Zone III, where larger fractions of Ag are available for sputtering, the increasing of the studied parameters already perceivable in Zone II becomes steeper. Thus, it is possible to state that both deposition rate and target potential exhibit an overall increasing tendency with increasing areas of Ag exposed in the Ti target. This expected behaviour was explained by Depla et al. [35-37], where the authors studied the effect of several parameters in the ion induced secondary electron emission coefficient (ISEE). One of the referred parameters is the target material dependency of the discharge voltage. At constant current and pressure – corresponding to the conditions used in this work for the preparation of the Ag:TiN coatings – the average ISEE coefficients of the used target materials (Ti and Ag) are rather close, 0.114 and 0.110 respectively. However, based on the Thornton relation [38], it is known that the discharge voltage is inversely proportional to the ISEE coefficient of the target material. It is also known that the ISEE coefficients are much higher for compounds (nitrides, oxides) than for metals [39-42], and consequently, some poisoning of the Ti fraction by formation of a thin TiN layer is not to be excluded. This means that the ISEE coefficient for Ti will, for sure, be higher than the one stated above for the metallic mode condition (as a result of the TiN poisoning of the Ti fraction of the composite target), while Ag ISEE coefficient should remain constant, since the formation of AgN is highly improbable thermodynamically, due to the fact that the sputtering of Ag in the presence of nitrogen has an extremely low reactivity [43]. To summarize, an increasing fraction of Ag in the Ti target will gradually reduce the effect of the poisoning of the Ti fraction of

the target (as less area of Ti is available for sputtering), causing a gradual increase of the target potential. This effect, summed with the lower Ag ISEE coefficient – which means that the discharge voltage of Ag is higher than that of Ti due to the inverse proportionality stated before – gives rise to the observed increase of the target potential from ~360 V (low Ag fraction) to ~410 V (high Ag fraction).

Since the amount of material that is deposited in the substrate per unit of time is correlated with the amount of atoms sputtered from the target, the explanations given above can also, in part, justify the evolution of the sputtering rate, as the decrease of the poisoned Ti fraction of the compound Ti/Ag target should increase the sputtering rate. In fact, Zone I and Zone II coatings exhibit rather low deposition rates, indicating that the compound target condition has the main role, while the Zone III ones were obtained with higher deposition rates. This must be due to the fact that the Ag fraction in the compound Ti/Ag target is high enough to somewhat deplete the poisoning effect of the Ti fraction responsible for the low sputtering rates, present both in Zone I and Zone II.

In a review paper, Smentkowski [44] explained the theoretical concept of sputtering yield, which can be defined by:

$$Y = \Lambda \, Fd_{(Eo)} \quad (1)$$

where Λ contains all of the material properties such as the surface binding energies (which is lower for Ag 3d than that of Ti 2p [45]) and $Fd_{(Eo)}$ is the density of energy deposited at the surface, depending on the mass, energy, and direction of the incident ion as well as the composition of the target. As the other deposition parameters were maintained constant during all depositions in the present work, the composition of the target is of paramount importance to explain the influence of the sputtering yield on the evolution of the sputtering rate. Furthermore, and since the surface binding energy of Ag is lower than that of Ti, the sputtering yield follows the inverse relation. Smentkowski data [44] show experimental and calculated Ag sputtering yields almost seven times higher than Ti (~2.5 and ~0.35 respectively for 400 eV Xe radiation). Consequently, with increasing Ag fraction in the Ti/Ag target an increase of the deposition rate is expected, once the TiN thin

layer poisoning effect is depleted and Ag sputtering yield (and binding energy) is higher than for Ti.

3.2. Composition of the as-deposited samples

The evolution of the deposition rate and target potential, as well as the increase of Ag fraction in the target will also be correlated with changes in the composition of the films. Figure 2a) shows the Ag chemical composition (at. %) results and the Ag/(Ti+N) ratio of the Ag:TiN coatings obtained from RBS spectra analysis, while Figure 2b) exhibits the ternary phase diagram of the deposited samples. Once again, the same three distinct zones are perceivable. Due to the very low area of Ag available for sputtering, the Ag content in the films from Zone I is also very low. Besides TiN reference coating (N/Ti ratio ~1), only one sample doped with Ag (~0.1 at. %) is ascribed to this zone. Both deposition rate and target potential are quite low in this zone (which can also explain the low incorporation of Ag), but also in Zone II. However, in this zone, one can observe an almost linear steep increase of Ag incorporation in the coatings with the increase of Ag fraction in the Ti/Ag target. This could mean that the much higher Ag sputtering yield is taking control over the composition evolution process, as the Ag content in this area increases steadily from ~4 at. % to ~35 at. % Ag with the increasing area of Ag (number of Ag pellets) available for sputtering in the target. As for Zone III films, the increase of Ag content is somewhat less steep than in Zone II, with Ag concentrations ranging from ~35 at. % to ~45 at. %, indicating that probably some kind of Ag saturation is being attained. This is quite clear taking into account the results exhibited by the last two samples, where Ag concentration is practically constant (~45 at. %). Regarding the Ag/(Ti+N) ratio, it directly correlates with the Ag content evolution, exhibiting an almost identical linear increase with increasing Ag fraction in the target. To note that the last two samples from Zone III, despite having similar Ag contents, do not present the same Ag/(Ti+N) ratio, indicating that, most probably, the N/Ti ratio (initially ~1) is not constant. As Ag fraction in the Ti/Ag target increases and Ti fraction decreases as the Ag pellets are being placed on the Ti erosion track, this result is somewhat expected. In fact, by taking a closer look at Figure 2b), it is

possible to see that N/Ti stoichiometry gradually changes to close-stoichiometry or even sub-stoichiometry almost throughout all coatings, with ratios very close to 0.8-1. For the highest Ag concentrations, however, a steep decrease of the N/Ti ratio is observable, with values close to 0.3-0.5. In fact, Ti contents decrease steadily from 50 at. % to ~30 at. %, while N concentrations initially also decrease steadily from ~50 at. % to ~25 at. %, but then an abrupt decrease is observable, with values close to 11-15 at. %. This abrupt fall of N concentration causes the deposited films to change from stoichiometric to under-stoichiometric Ag-doped TiN. Due to Ag low ISEE and high sputtering yield, as the Ag fraction in the target is continuously increased, the amount of species (mainly Ag) present in the reactor also increase, leading to a strong decrease on its mean free path. As no substrate bias voltage was used during the sputtering process, the available amount of nitrogen cannot be easily absorbed in the growing films due to mobility constraints [14].

3.3. Electrical and Thermal properties: analysis and discussion

As stated before, one of the main requirements to develop a coating system that may be suitable for EEG-type applications is its good conductivity. Figure 3 shows the plotted results of the resistivity variation with increasing Ag/(Ti+N) ratios. Once again, the three-zone behaviour is patent in the resistivity evolution. As expected, due to the low Ag incorporation, Zone I samples exhibit high resistivity values (between ~175-200 μΩ.cm), typical for stoichiometric TiN films [46]. In fact, one can consider that low Ag contents promote a small increase of resistivity, indication that Ag may be acting as an impurity. For intermediate Ag concentration in the coatings, resistivity decreases abruptly from ~200 to ~4.5 μΩ.cm, denoting that Ag, acting as a high conductivity dopant [23], promotes the desired effect for the envisaged application. Moreover, Zone III resistivity values are actually below the ones of bulk Ti (~45 μΩ.cm [47]). For the highest Ag content, a resistivity of ~0.4 μΩ.cm was attained.

To further investigate the electrical response of the films, the morphology of the deposited samples was studied by SEM. Figure 4 a_{1-3}) depicts the cross-section images, while Figure 4 b_{1-3})

shows the top view and Figure 4 c_{1-3}) the backscattered micrographs of the Ag-doped TiN films. The zone I films' high resistivity can be ascribed not only to the non-metallic characteristic of the low Ag content TiN-like coatings, but also to the well-known pyramid top columns [5] which, in turn, exhibit some degree of porosity and roughness. Non-uniform, rough and porous surfaces are known to hinder charge carrier mobility, thus reducing the films' conductivity. The low deposition rate patent in these Zone I films (see Figure 1) translate into lower thickness films, fact that can also explain the higher resistivity values. As for Zone II coatings (Figure 4 a_2-c_2) it is possible to see that the TiN matrix columns appear to become more disaggregated than in Zone I coatings, although a strong decrease in resistivity is visible. A steep incorporation of high conductivity Ag occurs within this Zone II, leading to the formation of Ag clusters/aggregates that extensively and uniformly cover the coating's surface. This result is consistent with the work of de los Arcos et al. [48] where the authors reported the formation of spherical Ag clusters embedded in the TiN matrix and also partially sitting on the surface. In fact, deep embedded clusters were also found in this work (Figure 4 c_2). So, as the Ag incorporation increases within Zone II, two phenomena occur: (i) the surface becomes more and more uniformly covered with the reported Ag clusters whereas (ii) the TiN matrix becomes increasingly embedded with smaller aggregates between its columns, thus strongly changing the samples resistivity behaviour from non-metallic to metallic. When the highest Ag concentration is attained – Zone III coatings, Figure a_3-c_3) – the morphology of the films changes dramatically. The columnar features are lost and the coatings develop a more granular, compact and rough morphology, similar to pure Ag thin films [49] (see Figure a_4 and b_4). This morphological change can be related to the fact already mentioned that the TiN matrix is gradually changing from stoichiometric to sub-stoichiometric as Ag concentration increases, which in turn also exhibits a granular-like compact structure [5]. The low resistivity of this zone's samples can be in part ascribed to the combination of these morphological changes, as the content of high conductivity Ag is quite substantial and the sputtered films are very compact, dense and thick, which are prerequisites to low resistivity values. To note that Ag clusters are still present in the coating's

surface (Figure 4 b_3), although smaller in size when compared to Zone II ones, but no embedded aggregates are visible (Figure 4 c_3). This could mean that some fraction of Ag may, perhaps, be dissolved in the N-deficient TiN matrix, opening the door to a possible formation of a TiAg intermetallic.

To further understand the growth mechanisms and the influence of the observed features patent in SEM observations in the resistivity evolution, a comprehensive structural characterization of the Ag-doped TiN samples was performed. Figure 5 shows the XRD diffractograms of the sputtered samples, taking into account their increasing Ag content. Once more, the three-zone behaviour is clearly visible, being in great accordance with all the analysis done above. A very close correlation between SEM observations and XRD data can, in fact, be claimed, with the Ag distribution in the TiN matrix playing a pivotal role in the overall behaviour. Taking a closer look at Figure 5 a), where the full range diffractograms are shown, Zone I comprises, once more, only the stoichiometric TiN reference sample and the low Ag content one (0.1 at. %). Both coatings are highly textured, exhibiting a preferential fcc TiN (111) growth (ICDD card no. 00-038-1420), typical for stoichiometric TiN films [5,14,46]. Two other peaks are also present at diffraction angles of ~62º – fcc TiN (220) – and ~78º – fcc TiN (222). No Ag peaks were detected in the 0.1 at. % Ag sample probably due to the fact that the amount of incorporated Ag (as well as its grain size) is too low to be detected [50]. The indistinguishable structural differences between these TiN-like coatings that comprise Zone I may justify the rather similar high resistivity values exhibited. As for Zone II coatings, the preferential growth remains the same as the one for Zone I films (fcc TiN (111)), although some changes are clearly visible. A new peak at ~42.5º corresponding to the fcc TiN (200) phase becomes perceivable from 20.2 at. % Ag contents onwards, while the fcc TiN (222) peak suffers a strong shift to lower diffraction angles for Ag contents ranging from 6.3 to 14.2 at. %, disappearing almost completely from 20.2 at. % onwards. In fact, also the main fcc TiN (111) peak suffers a shift to lower 2θ angles and also its intensity strongly decreases (see Figure 5 b), indicating that the TiN fcc structure is being progressively destroyed (strong amorphization) by the

formation of a new fcc Ag (111) phase (ICDD card no. 00-004-0783), as a new peak at ~38º becomes clear. The authors ascribe this peak to fcc Ag (111) as several pure Ag aggregates are visible sitting on the surface and embedded in the TiN matrix of Zone II coatings (see Figure 4). However, due to the fact that the tetragonal TiAg (111) peak (ICDD card no. 00-006-0560) occurs at approximately the same diffraction angle, the formation of a TiAg intermetallic (although unlikely once Zone II TiN matrix is stoichiometric or close-stoichiometric, with almost all interstitial sites occupied by N atoms) may not be excluded. Also, the slight shift towards lower 2θ angles referred above, may perhaps suggest small Ag inclusions in the TiN fcc structure. Zone II is, in fact, a transition zone strongly defined by a steep decrease of the resistivity values (see Figure 3), being now clear that the formation of a new highly conductive fcc Ag phase, in the form of clusters, sitting in the surface and embedded in an increasingly amorphous TiN matrix, plays a key role in the process. Gulbiński and Suszko [51] claimed that for high Ag contents, grain boundary segregation occurs, hindering the growth of the metallic nitride matrix, decreasing its crystallinity. Zone II and especially Zone III data are in accordance with this claim, as for higher Ag concentrations the sputtered films exhibit a very low degree of crystallinity, with very broad peaks and baseline noise clearly patent, as it is possible to see from Figure 5 b). To note that the fcc TiN (111) peak of the highest Ag concentration sample (47.5 at. %) exhibits a strong shift towards high diffraction angles, corroborating the assumption that the TiN matrix formed may be N-deficient, offering the possibility of some Ag atoms occupying interstitial sites (potential formation of TiAg intermetallics), thus exhibiting lower lattice parameters. These results are, as stated before, in great consistence with SEM observations (see Figure 4), where it is possible to see a gradual increase of the compactness of the films, with the organized columnar growth being progressively lost as the Ag content increases; and also with composition analysis (see Figure 2), confirming the formation of a N-deficient TiN matrix for high Ag contents. To summarize, the growth behaviour of the Ag-doped TiN films provides a coherent justification to the resistivity evolution. As Ag content increases, the TiN fcc structure is continuously hindered, while the formation of a new highly

conductive Ag fcc amorphous phase takes place (in fact, fcc Ag (111) phase becomes the preferential one for the highest Ag content). This means that, as stated above, the sputtered films are evolving from a nitride-based to a metallic-like character, thus exhibiting an overall decrease of the resistivity values.

In analytical terms, the resistivity of thin films can be expressed by the well-known Matthiessen's rule [52]:

$$\rho = \rho_p + \rho_m + \rho_f + \rho_i + \rho_s \quad (2)$$

where ρ_p, ρ_m, ρ_f, ρ_i and ρ_s represent the resistivity caused by scattering from phonons, impurities, defects, grain boundaries and the surface scattering, respectively. The scattering effect from impurities must not be considered, once no major impurities were detected in the composition analysis such as oxygen or argon inclusions. If present, their content should be within the standard error of the RBS technique, which is 3-4 at. %. Also, no important defects are perceivable in the coatings. Taking into account the Fuchs-Sondheimer (F-S) model [53-54], the resistivity contribution due to the scattering effect of conduction electrons at the film's surface should also be disregarded, as the surface scattering effect only becomes relevant when the film's thickness is below the mean free path of the conduction electrons. All sputtered Ag:TiN coatings exhibit thicknesses > 1 μm, thus being well above the electron mean free path of Ti and Ag, both in the range of tens of nanometres. Consequently, only the scattering from phonons and grain boundaries contributions should be taken into account, once the chemical composition of the samples is an important variable (already analysed) and the role of grain size evolution should also be fundamental. Mayadas et al. [55-56], in an attempt to improve the F-S model, postulated the Mayadas-Shatzkes (M-S) model that considers the dispersion of electrons by grain boundaries, assuming that the mean grain size, which is below the film thickness, is the main dispersive factor [57].

Consequently, the grain size evolution was investigated as a function of the Ag/(Ti+N) ratio, taking into account the predominant fcc TiN (111) and Ag (111) phases, as shown in Figure 6. It is

possible to see that small Ag incorporations – within Zone I films – translates into a decrease of the grain size when comparing with the stoichiometric TiN reference coating. To note that no Ag (111) phase was detected in the 0.1 at. % Ag sample. Although no differences were detected in the XRD diffractograms, small additions of Ag have a profound effect on the grain size of the growing Zone I films, decreasing from ~37 nm to ~22 nm. Once more, the rather high TiN-like resistivity values that are exhibited by low-Ag concentration samples are in great accordance with grain size data, once it is known that grain size evolution has an inverse proportionality in regard to resistivity [47], meaning that a decrease in grain size is supposed to give raise to an increase of resistivity. As for Zone II films, the previous relation is also valid, once a substantial increase of grain size values (until ~75 nm and ~30 nm for TiN (111) and Ag (111) phases, respectively) for the first samples within zone – 6.3-14.2 at. % Ag – gives raise to a strong decrease of resistivity. This is also consistent with XRD data, once it is possible to see (Figure 5 b) a slight increase of both fcc TiN (111) and Ag (111) peaks' intensity and definition, indicating an improvement of the crystallinity of the films, thus leading to low resistivity values. However, from 20.2 at. % Ag onward, a progressive amorphization of the coatings take place (as explained before) until the films are almost amorphous – Zone III –, fact that is proven by the accentuated decrease of grain size from ~75 nm to ~15 nm for fcc TiN (111) phase and from ~30 nm to ~10 nm for fcc Ag (111). Therefore, with such strong decrease of crystallinity, it was expected an increase of the resistivity values. In fact, the complete opposite is happening, once the resistivity values continue to decrease in Zone III, although slightly. This could mean that the main contribution to resistivity may not be grain boundary scattering, but scattering from phonons instead (due to the strong composition changes evidenced throughout the range of sputtered Ag:TiN films), confirming the paramount importance of Ag incorporation as the main controling mechanism of the exhibited behaviour throughout all characterization performed. As claimed before, all evidences show that the coatings are steadily changing from a nitride/compound-like (Zone I) to a metallic-like (Zone III) behaviour with a transition zone (Zone II) in between.

Modulated IR Radiometry – Principles and Measurement Technique

When a material is excited with an intensity-modulated energy beam (e.g. laser), a periodic IR emission will take place as a consequence of the thermal relaxation processes that occur in the material. Modulated IR Radiometry (MIRR) is basically a non-destructive measurement technique, sensitive to that periodic IR emission. Usually the concept of "thermal waves" is associated with the technique, due to the periodic characteristic of the thermal response. In this particular work, an intensity-modulated laser beam heating was applied, and the resulting periodic IR emission was detected and interpreted to determine the thermal transport parameters of the TiN/Ag thin films, namely the thermal effusivity, the thermal diffusion time, from which other thermal parameters which are relevant for time-dependent surface heating processes of coatings can be calculated.

4. CONCLUSIONS

ACKNOWLEDGEMENTS

This research is partially sponsored by FEDER funds through the program COMPETE – Programa Operacional Factores de Competitividade and by national funds through FCT – Fundação para a Ciência e a Tecnologia, under the projects PEst-C/EME/UI0285/2011, PTDC/SAU-ENB/116850/2010, PTDC/CTM-NAN/112574/2009 and Programa Pessoa 2012/2013 Cooperação Portugal/França, Project nº 27306UA Porous architectures in GRAded CERamic thin films for biosensors - GRACER. The authors would also like to acknowledge CEMUP for SEM analysis. P. Pedrosa acknowledges FCT for the Ph.D. grant SFRH/BD/70035/2010.

BIBLIOGRAPHY

1. M. Teplan**,** Measurement Science Review 2 (2) (2002).
2. E. McAdams, "Bioelectrodes," in Encyclopaedia of Medical Devices and Instrumentation, Webster J. G. Ed., New York, Wiley, (1988) 120.
3. A. Searle, L. Kirkup, Physiolog. Meas. 22 (2000) 71.
4. W. K. Ko, J. Hynecek, Dry electrodes and electrode amplifiers: in H.A. Miller and D.C. Harrison (Eds), Biomedical Electrode Technology, Academic Press, N.Y. (1974).
5. L.T. Cunha, P. Pedrosa, C. J. Tavares, E. Alves, F. Vaz, C. Fonseca, Electrochimica Acta, Vol. 55, nº 1, pp. 59-67, 2009.
6. G. Gargiulo, R. A .Calvo, P. Bifulco, M. Cesarelli, C. Jin , A. Mohamed , A. van Schaik, Clin. Neurophysiol, 121 (5), 686-93 (2010).
7. C. Fonseca, J. P. Silva Cunha, R. E. Martins, V. Ferreira, J. P. Marques de Sá, M. A. Barbosa, A. Martins Silva, IEEE Trans. Biomed. Eng. 54 (1), 162-165 (2007).
8. K.-P. Hoffmann and R. Ruff, Proceedings of the 29th Annual International Conference of the IEEE EMBS, Lyon, France, August 23-26, 2007.
9. J. Baek, J. An, J. Choi, K. Park, S. Lee, Sensors and Actuators A, 143, 423–429 (2008).
10. A. Gruetzmann, S. Hansen, J. Muller, Physiol. Meas. 28, 1375–1390 (2007).
11. V. Marozas, A. Petrenas, S. Daukantas, A Lukosevicius, Journal of Electrocardiology 44 (2011) 189–194.
12. A. Martins Silva, IEEE Trans. Biomed. Eng. 54 (1) 2007, 162-165.
13. S. Piscanec, L. Ciacchi, E. Vesselli, G. Comelli, O. Sbaizero, S. Meriani, A. De Vita, Acta Materialia 52 (2004) 1237.
14. P. Pedrosa, E. Alves, N. P. Barradas, P. Fiedler, J. Haueisen, F. Vaz, C. Fonseca, Corrosion Science 56 (2012) 49–57.
15. S. L. Chui, J. Leu, P. S. Ho, J. Appl. Phys. 76, 5136 1994.
16. O. Kraft, M. Hommel, E. Arzt, Mater. Sci. Eng., A 288, 209 2000.
17. M. Hommel, O. Kraft, Acta Mater. 49, 3935 2001.
18. B. E. Alaca, M. T. A. Saif, H. Sehitoglu, Acta Mater. 50, 1197 2002.
19. D. Y. W. Yu, F. Spaepen, J. Appl. Phys. 95, 2991 2003.
20. S. P. Lacour, S. Wagner, Z. Huang, Z. Suo, Appl. Phys. Lett. 82, 2404 2003.
21. Y. Xiang, T. Li, Z. Suo, J. Vlassak, Appl. Phys. Lett. 87, 161910 2005.
22. R. M. Niu, G. Liu, C. Wang, G. Zhang, X. D. Ding, J. Sun, Appl. Phys. Lett. 90, 161907 2007.
23. R. X. Wang, X. M. Tao, Y. Wang, G. F. Wang, S. M. Shang, Surf. & Coat. Technol. 204 (2010) 1206–1210.

24. R. C. Adochite, D. Munteanu, M. Torrell, L. Cunha, E. Alves, N. P. Barradas, A. Cavaleiro, J. P. Riviere, E. Le Bourhis, D. Eyidi, F. Vaz, Appl. Surf. Sci. 258 (2012) 4028–4034.
25. H. Chiriac, M. Urse, F. Rusu, C Hison, M. Neagu, Sensors and Actuators 76 (1999) 376-380.
26. K.-H. Liao, K.-L. Ou, H.-C. Cheng, C.-T. Lin, P.-W. Peng, Appl. Surf. Sci. 256 (2010) 3642-3646.
27. M. Fiori, M. Paula, A. Bernardin, H. Riella, E. Angioletto, Materials Science and Engineering C 29 (2009) 1569–1573.
28. M. Santos, C. Oliveira, C. Tachinski, M. Fernandes, C. Pich, E. Angioletto, H.G. Riella, M. Fiori, International Journal of Mineral Processing 100 (2011) 51–53.
29. P. J. Kelly, H. Li, K. A. Whitehead, J. Verran, R. D. Arnell, I. Iordanova, Surf. & Coat. Technol. 204 (2009) 1137–1140.
30. P. J. Kelly, H. Li, P. S. Benson, K. A. Whitehead, J. Verran, R. D. Arnell, I. Iordanova, Surf. & Coat. Technol. 205 (2010) 1606–1610.
31. L. A. Geddes, L. E. Baker, A. G. Moore, Med. & Biol. Eng.. Vol. 7, pp. 49-56, Pergamon Press, 1969.
32. N. P. Barradas, C. Jeynes, R. P. Webb, Appl. Phys. Lett. 71 (1997) 291.
33. A. F. Gurbich, Nucl. Instr. and Meth. B 268 (2011) 1703H. A. Wriedt, J. L. Murray, Bull. Alloy Phase Diagrams, 8/4 (1987) 378.
34. L. J. van der Pauw, Philips Res. Repts. 13, 1-9, 1958.
35. D. Depla, S. Heirwegh, S. Mahieu, J. Haemers, R. De Gryse, J. Appl. Phys. 101, 013301 (2007).
36. D. Depla, G. Buyle, J. Haemers, R. De Gryse, Surf. & Coat. Technol. 200 (2006) 4329– 4338.
37. D. Depla, S. Mahieu, R. De Gryse, Thin Solid Films 517 (2009) 2825–2839.
38. P. Riccardi, M. Ishimot, P. Barone, R. A. Baragiola, Surf. Sci. 571, L305 (2004).
39. J. M. Chappé, F. Vaz, L. Cunha, C. Moura, M. C. Marco de Lucas, L. Imhoff, S. Bourgeois, J.F. Pierson, Surf. & Coat. Technol. 203 (2008) 804-807.
40. J. Borges, F. Vaz, L. Marques, Appl. Surf. Sci. 257 (2010) 1478–1483.
41. J. Borges, N. Martin, N. P. Barradas, E. Alves, D. Eyidi, M. F. Beaufort, J. P. Riviere, F. Vaz, L. Marques, Thin Solid Films 520 (2012) 6709–6717.
42. R. Arvinte, J. Borges, R. E. Sousa, D. Munteanu, N. P. Barradas, E. Alves, F. Vaz, L. Marques, Appl. Surf. Sci. 257 (2011) 9120– 9124.
43. J. F. Pierson, D. Wiederkehr, A. Billard, Thin Solid Films 478 (2005) 196–205.
44. V. S. Smentkowski, Progress in Surface Science 64 (2000) 1-58.

45. C. D. Wanger, W. M. Riggs, L. E. Davis, J. F. Moulder, G. E. Muilenberg, Handbook of X-ray Photoelectron Spectroscopy, Perkin-Elmer Corp., Physical Electronics Division, Eden Prairie, Minnesota, USA, 1979.
46. F. Vaz, J. Ferreira, E. Ribeiro, L. Rebouta, S. Lanceros-Méndez, J. A. Mendes, E. Alves, Ph. Goudeau, J. P. Rivière, F. Ribeiro, I. Moutinho, K. Pischow, J. de Rijk, Surf. & Coat. Technol. 191 (2005) 317–323.
47. M. E. Day, M. Delfino, J. A. Fair, W. Tsai, Thin Solid Films 254 (1995) 285-290.
48. T. de los Arcos, P. Oelhafen, U. Aebi, A. Hefti, M. Düggelin, D. Mathys, R. Guggenheim, Vacuum 67 (2002) 463–470.
49. Y. Xiong, H. Wu, Y. Guo, Y. Sun, D. Yang, D. Da, Thin Solid Films 375 (2000) 300-303.
50. J. G. Han, H. S. Myung, H. M. Lee, L. R. Shaginyan, Surf. & Coat. Technol., 163-164 (2003) 591-596.
51. W. Gulbiński, T. Suszko, Surf. & Coat. Technol., 201 (2006) 1469–1476.
52. K.-Y. Chan, T.-Y. Tou, B.-S. Teo, Microelectronics Journal ,37 (2006) 608-612.
53. K. Fuchs, Proc. Camb. Philos. Soc., 34 (1938) 100.
54. E. H. Sondheimer, Phys. Rev., 80 (1950) 401.
55. A. F. Mayadas, M. Shatzkes, J. F. Janak, Appl. Phys. Lett., 14 (1969) 345.
56. A. F. Mayadas, M. Shatzkes, Phys. Rev. B, 1 (1970) 1382.
57. J. M Camacho, A. I. Oliva, Microelectronics Journal, 36 (2005) 555-558.

Table captions

Table I. Experimental parameters used in all depositions.

Deposition parameters	
Ar (Pa)	3×10^{-1}
N_2 (Pa)	3.4×10^{-2}
t (s)	3600
I ($A.cm^{-2}$)	$1x10^{-2}$
T (ºC)	100
Bias (V)	GND
P_{work} (Pa)	$\sim4\times10^{-1}$
P_{base} (Pa)	$\sim10^{-4}$

Figure captions

Fig. 1. Evolution of the deposition rate and target potential with increasing area of Ag exposed in the target.

Fig. 2. Evolution of the coatings' Ag content and Ag/(Ti+N) ratio as a function of the area of Ag exposed in the target (a) and Ti-N-Ag composition ternary phase diagram (b).

Fig. 3. Coatings' resistivity evolution with increasing Ag content and Ag/(Ti+N) ratio.

Fig. 4. SEM cross-section (a_{1-4}), top (b_{1-4}) and backscattered (c_{1-3}) micrographs of the Ag-doped TiN and pure Ag coatings.

Fig. 5. XRD diffractograms as a function of Ag incorporation in the coatings; (a) full scale diffractograms and (b) 34-40º magnification.

Fig. 6. Grain size evolution with increasing Ag/(Ti+N) ratio.

Fig. 7.

Figure 1

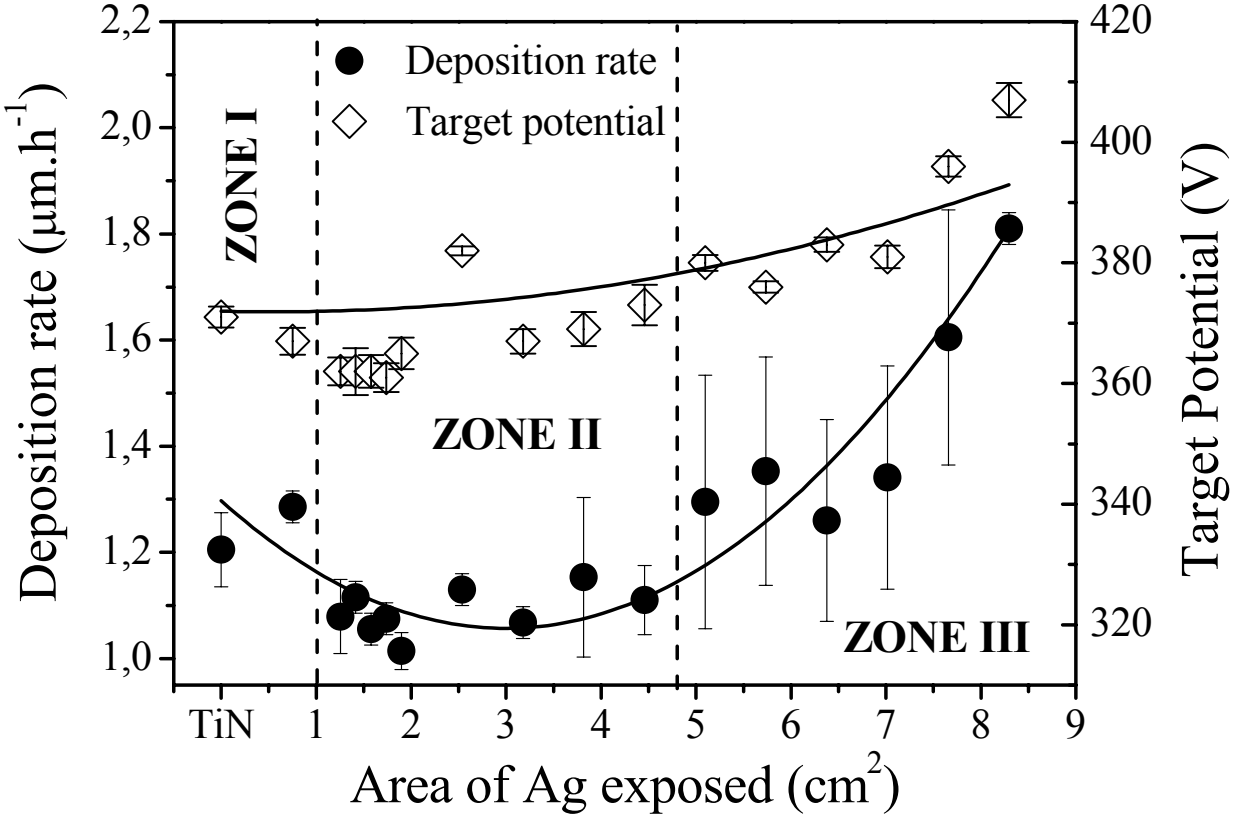
Deposition rate
Target potential
ZONE I
ZONE II
ZONE III
Deposition rate (µm.h-1)
Target Potential (V)
Area of Ag exposed (cm2)
TiN
2,2
2,0
1,8
1,6
1,4
1,2
1,0
420
400
380
360
340
320
1
2
3
4
5
6
7
8
9

Figure 2

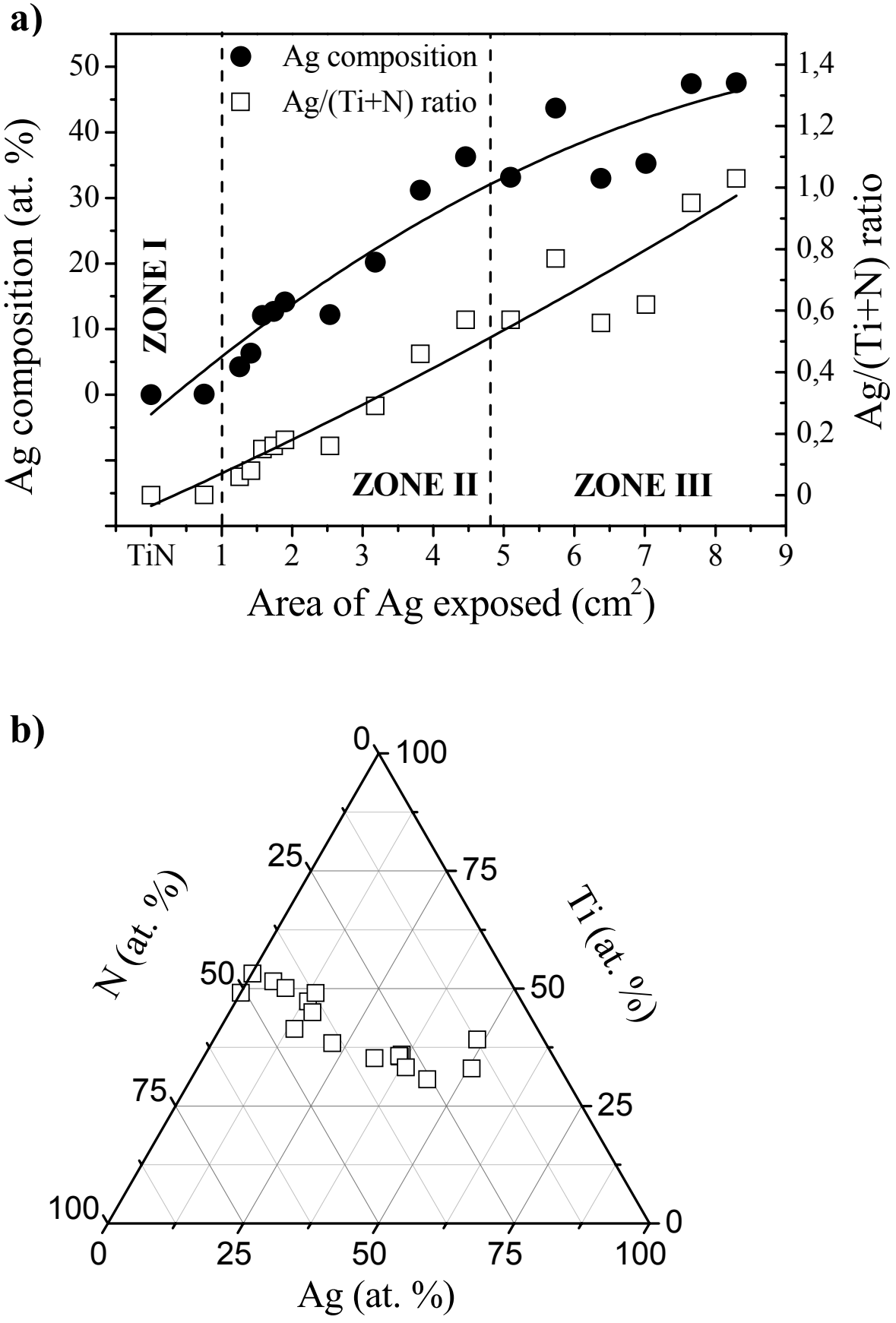
a)
Ag composition
Ag/(Ti+N) ratio
ZONE I
ZONE II
ZONE III
Ag composition (at. %)
Ag/(Ti+N) ratio
Area of Ag exposed (cm2)
TiN
b)
N (at. %)
Ti (at. %)
Ag (at. %)

Figure 3

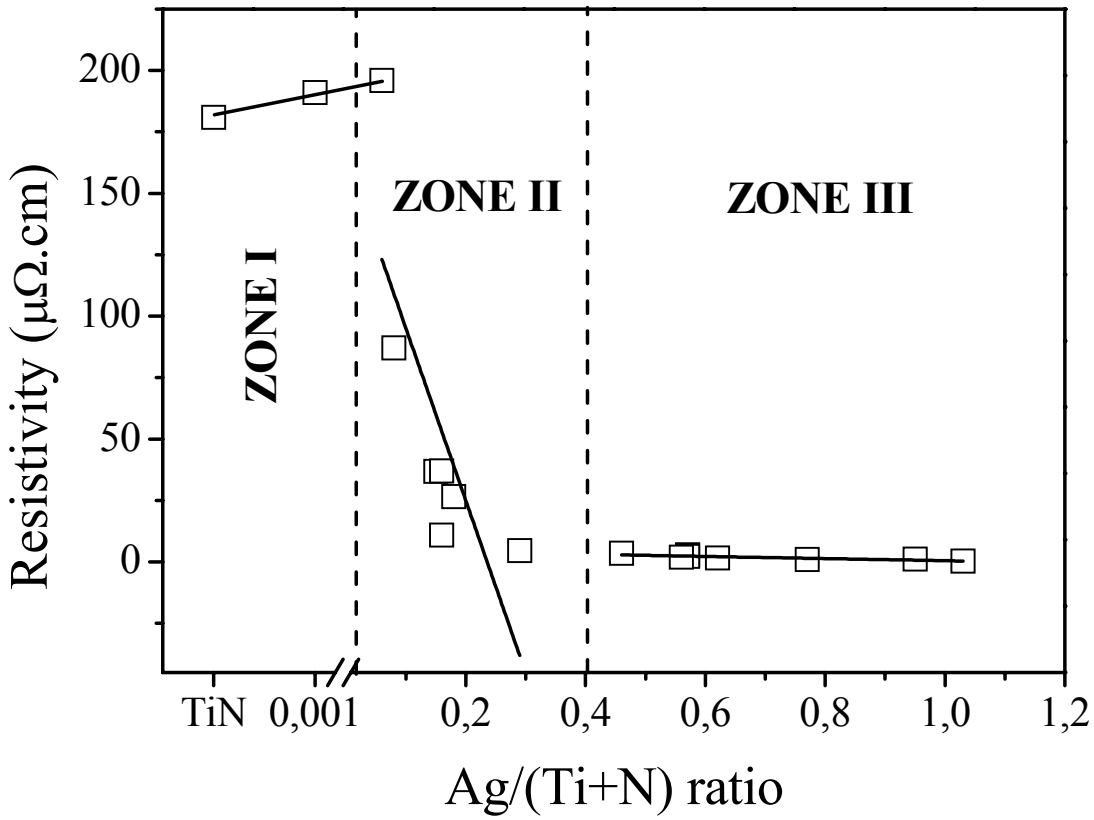
Resistivity (μΩ.cm)
200
150
100
50
0
ZONE I
ZONE II
ZONE III
TiN
0,001
0,2
0,4
0,6
0,8
1,0
1,2
Ag/(Ti+N) ratio

Figure 4

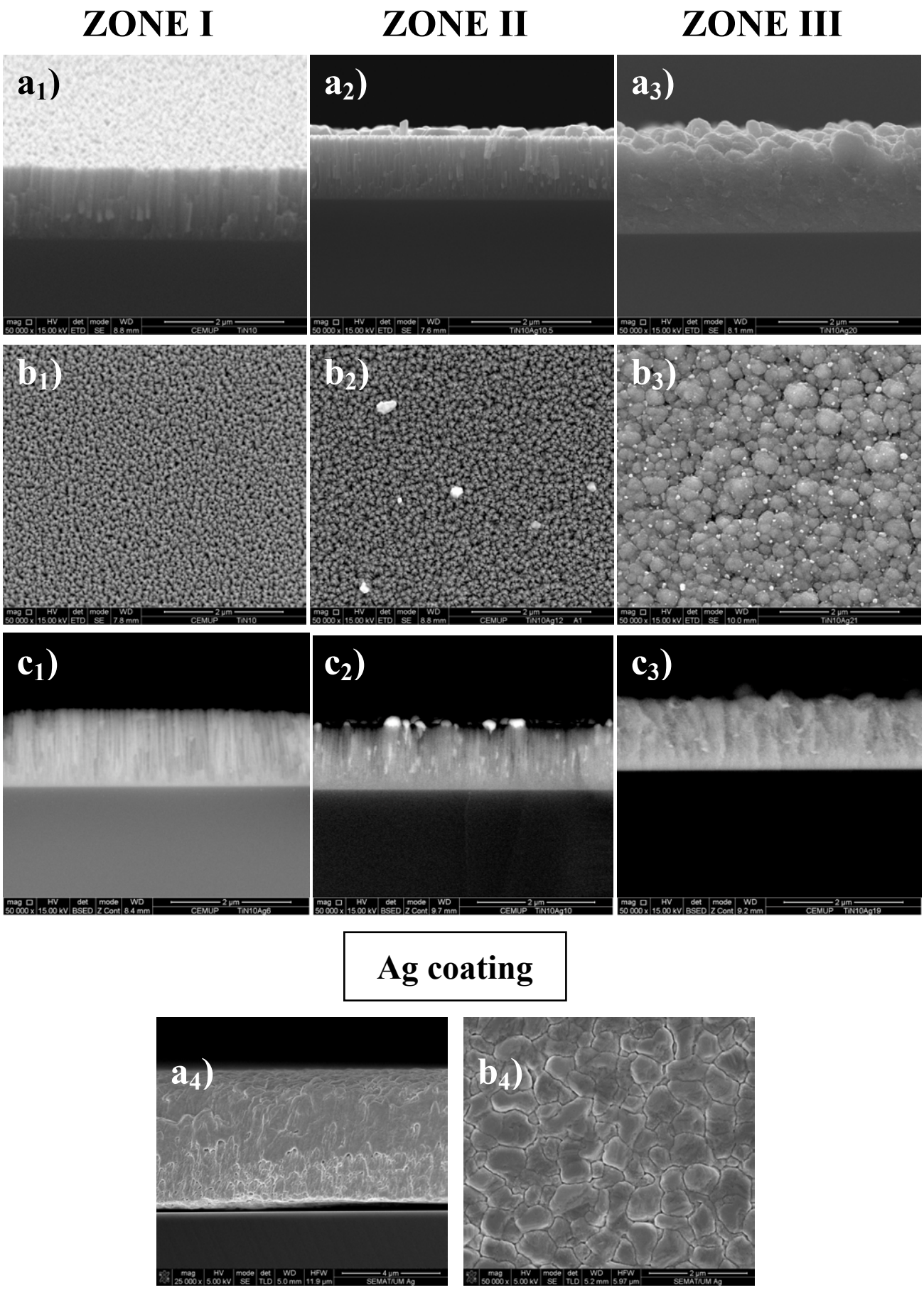

Figure 5

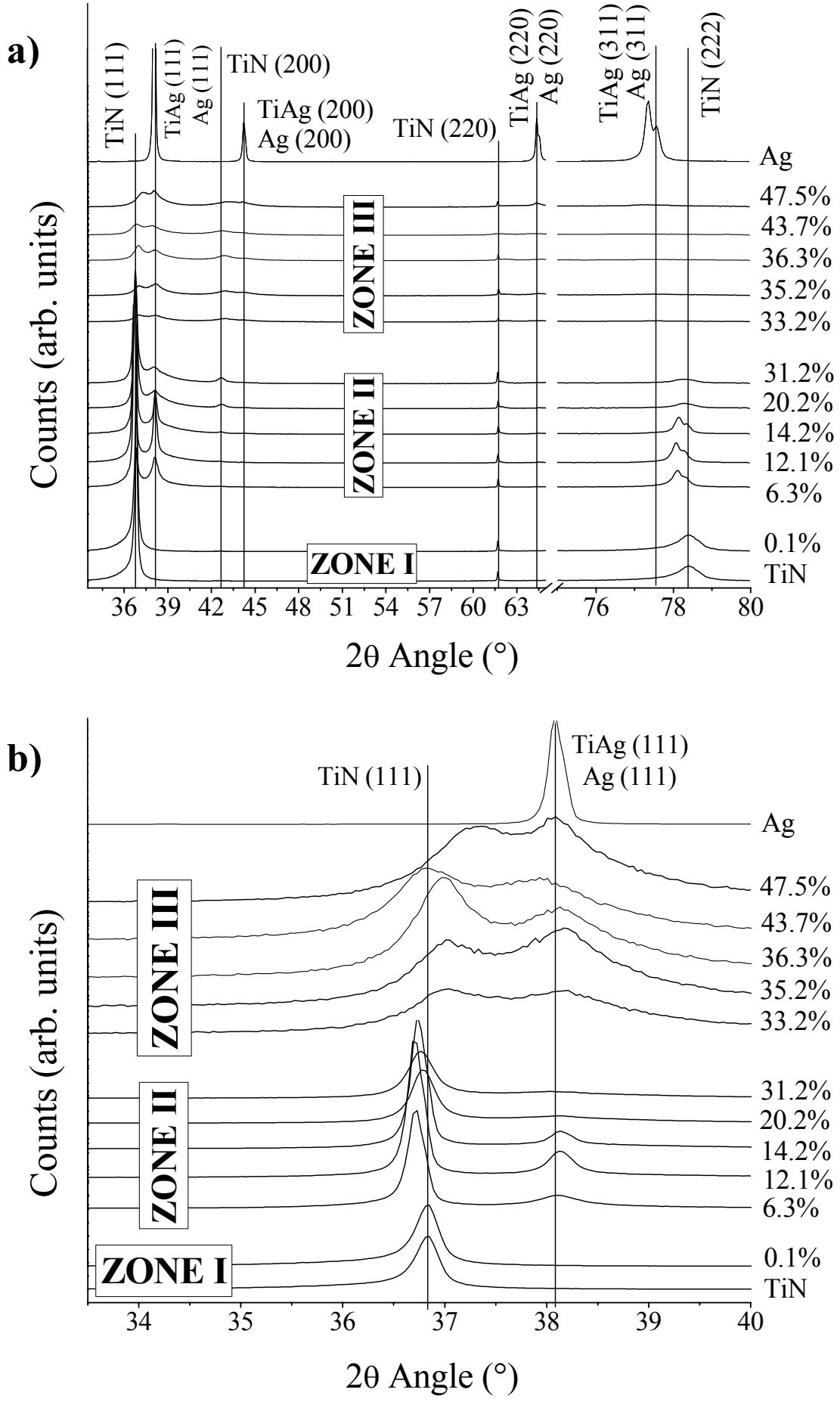
a)
TiN (111)
TiAg (111)
Ag (111)
TiN (200)
TiAg (200)
Ag (200)
TiN (220)
TiAg (220)
Ag (220)
TiAg (311)
Ag (311)
TiN (222)
ZONE III
ZONE II
ZONE I
Ag
47.5%
43.7%
36.3%
35.2%
33.2%
31.2%
20.2%
14.2%
12.1%
6.3%
0.1%
TiN
Counts (arb. units)
36 39 42 45 48 51 54 57 60 63 76 78 80
2θ Angle (°)
b)
TiN (111)
TiAg (111)
Ag (111)
ZONE III
ZONE II
ZONE I
Ag
47.5%
43.7%
36.3%
35.2%
33.2%
31.2%
20.2%
14.2%
12.1%
6.3%
0.1%
TiN
Counts (arb. units)
34 35 36 37 38 39 40
2θ Angle (°)

Figure 6

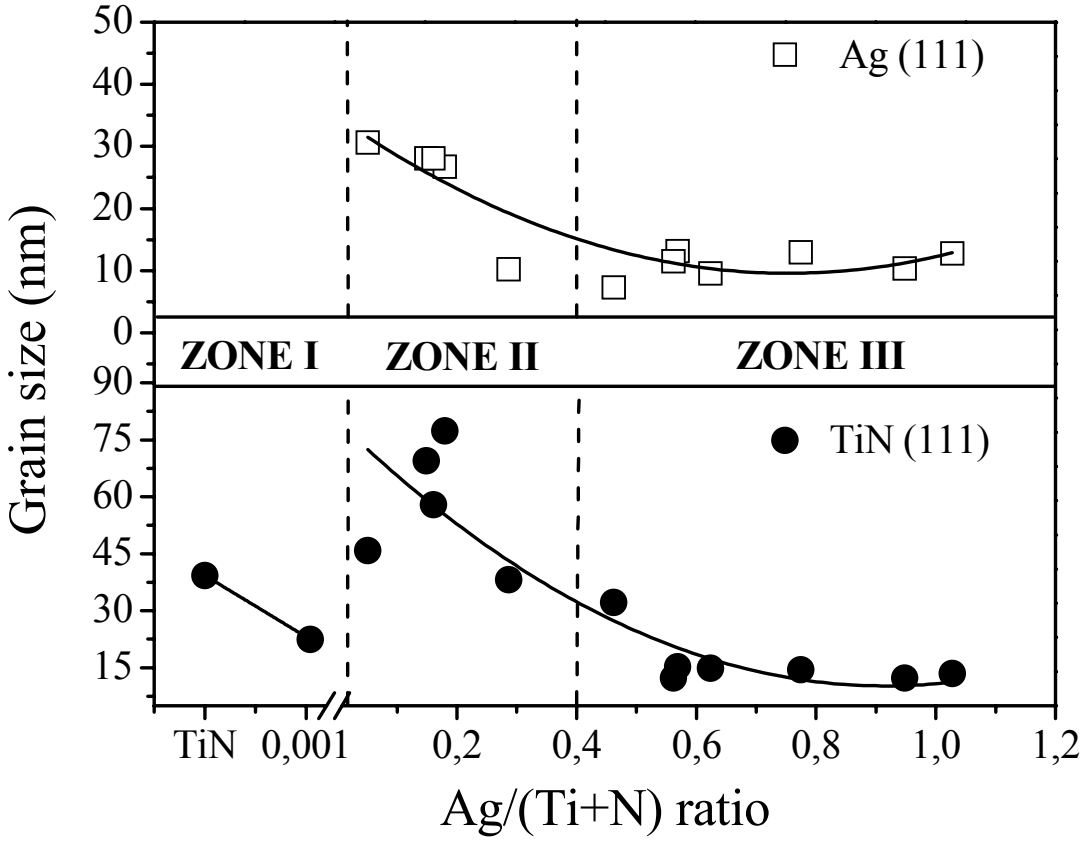
Grain size (nm)
Ag (111)
TiN (111)
ZONE I
ZONE II
ZONE III
TiN
0,001
0,2
0,4
0,6
0,8
1,0
1,2
Ag/(Ti+N) ratio

Figure 7